A comparative study of pool boiling heat transfer in different porous artery structures

Kai Zhang[a], Lizhan Bai[a], Haichuan Jin[a], Guiping Lin[a], Dongsheng Wen[a, b,*]

[a]Laboratory of Fundamental Science on Ergonomics and Environmental Control, School of Aeronautic Science and Engineering, Beihang University, Beijing 100191, PR China

[b]School of Chemical and Process Engineering, University of Leeds, Leeds, LS2 9JT, UK

Abstract: A novel porous artery structure is proposed to enhance the pool boiling heat transfer performance based on the concept of "phase separation and modulation". In the experiment, multiple rectangular arteries were sintered directly in the bottom of a porous structure, and a thin copper microporous layer were placed between the heating surface and the rectangular arteries. Compared with conventional porous structure, this multi-layer porous artery structure proposed here can effectively improve the pool boiling heat transfer performance due to the high-density nucleation sites, capillary-induced liquid replenishment, and the liquid/vapor phase separation. According to the experimental study, favorable results have been reached as expected, a 200% higher CHF, a 144% higher heat transfer coefficient (HTC) as well as a 59% lower superheat at the onset of nucleate boiling (ONB) were demonstrated, compared with the boiling heat transfer on a plain surface. In addition, the effects of the top and bottom microporous layer thickness and the artery depth on the pool boiling heat transfer performance were investigated, and the inherent physical mechanisms were analyzed and discussed.

Keywords: pool boiling; porous structure; critical heat flux; experiment

1 Introduction

As a highly efficient heat transfer mode, pool boiling has been applied in a wide variety of areas ranging from large scale electric power generation, thermal energy storage, desalination systems and refrigeration units to small compact systems such as sterilization and electronics cooling [1–3]. During the pool boiling process, the heat transfer proceeds mainly in the form of liquid/vapor phase change with the transfer of the latent heat, which can dissipate a large amount of heat with relatively small temperature difference between the heating surface and the bulk fluid, i.e.,.

For pool boiling on a plain surface, the heat transfer coefficient (HTC) increases gradually with the heat flux. However, when the heat flux reaches a threshold value, i.e., the so-called critical heat flux (CHF), a vapor film would develop between the heating surface and the liquid, severely deteriorating the heat transfer performance. This phenomenon is also termed as the boiling crisis, which is accompanied by a rapid increase of heating surface temperature, leading to a catastrophic burn-out of the devices to be cooled. It is well recognized that the CHF is the chief limiting factor for pool boiling on a plain surface, and also the main design parameter to consider for many industrial applications. How to increase HTC and CHF of pool boiling has received consistent interest for a long time.

Extensive experimental and theoretical researches have been conducted to improve the pool boiling heat transfer performance. The most well-known CHF model for nucleate boiling at a smooth horizontal surface was derived from the hydrodynamic instability theory, first proposed by Zuber [4] and modified by Dhir [5]. They assumed that once the velocity of escaping vapor columns reached a threshold value, the instability of the vapor columns would form a vapor

blanket over the boiling surface that prevent the direct contact of the liquid with   the boiling

surface.   The hydrodynamic model focuses on the bulk fluid effect, and was shown to be in

agreement with some experimental CHF results on plain surfaces. However it cannot explain

the near-surface effects such as surface wettability [6-9], contact angle [10-13], surface

roughness [14, 15], and surface capillarity[16-19], etc.

The improvement of CHF has been progressed along two directions by multiscale surface

engineering, i.e., employing macroscale structures to address the hydrodynamic instability issue

by actively modulating the characteristic length, and using microscale structures to improve

capillary-induced effects to increase the liquid replenishment effects [34]. The competition

between vapor escaping from the surface and liquid replenishment would decide the occurrence

of CHF. For the past several decades, many measures have been proposed to intensify the near-

surface effects both theoretically [20-21] and experimentally, including surface coating [18, 22-

28] to modify the surface wettability and contact angle, 2D or 3D porous structure [29-39] to

enhance the capillary effect and nano/mirco channel surface [40-48] to change the geometrical

morphology of the boiling surface.

In particular, the employment of porous medium with micro/nano features   has been shown

to yield significant improvement in the pool boiling heat transfer performance. For instance,

Liter and Kaviany [22] employed a modulated porous-layer coating surface with periodically

non-uniform thickness to enhance the pool boiling heat transfer performance. Experimental

results showed that the pool boiling CHF was enhanced to nearly three times of that on a plain

surface. Li and Peterson[16][49] experimentally examined the pool boiling CHF and HTC on

several uniform and modulated porous structures made of sintered copper particles. The

modulated porous structure could reach a CHF of about 450 W/cm^2, which was about three times of that on a plain surface. Xxx a few sentences of why chf increase. However it is rather difficult to further enhance the pool boiling CHF by using the uniform or modulated porous structures, because the escaping bubbles impede the replenishment of the liquid to the boiling surface, causing insufficient liquid supply and the resultant occurrence of the CHF.

Very recently, we proposed an innovative concept of "phase separation and modulation", by using porous artery structures that allow the liquid replenishment and vapor escaping from the heating surface to have two different paths. In this novel structure, the capillary forces developed in the microporous structure adjacent to the heating surface allows the sufficient liquid wetting to the surface, and the artery structures permit vapor flow-out , thus significantly reducing the liquid/vapor counter flow during the pool boiling. The proof-of-concept has been …. A few sentences review of our published papers. However, the experimental data also showed the drawback for this structure, i.e., the wall superheat became very large at very high heat fluxes. The deterioration in the heat transfer performance should be attributed to significantly reduced effective heat transfer area due to the existence of the vapor channels in the copper pillar. In order to obtain better heat transfer performance especially at high heat fluxes, we designed and fabricated the test samples C and D. In this work, we further advanced the concepts by designing and comparing the effects of different porous artery structures. Four different structures are designed, including xx. The pool boiling heat transfer performance mainly including the HTC and CHF for different structures are experimentally studied, evaluated and compared, as well as the revelation of inherent physical mechanisms.

2 Experimental setup

2.1 Preparation of test samples

In this work, high purity (>99.99%) spherical copper particles were used to prepare the copper porous structures, due to the high thermal conductivity of copper. The copper particles were prepared by gas atomization with an average particle size of ~100 micron. The copper particles were first put into a well prepared graphite mold, and placed in a vacuum sintering stove with a high temperature of 800 ℃ for several hours to form the porous structure. Each test sample was cleaned in an ultrasonic bath with 20% citric acid, absolute ethyl alcohol and de-ion water for 10 min respectively. All the copper pillars were made of C1020 oxygen-free copper, whose surfaces with direct contact with the copper porous structure were initially polished by using abrasive papers to have an almost mirror finish. The copper pillars were cleaned by ultrasonic cleaners immersed in acetone, and then rinsed carefully with pure water at the ambient temperature. These copper pillars and the copper porous structures were connected by direct sintering in the vacuum sintering stove, to form different test samples in the experiments.

The porosity Φ of the copper porous structures can be estimated as follows:

$$\Phi = 1 - \frac{m_1}{\rho_1 v} \tag{1}$$

where m_1 is the mass of the test samples, ρ_1 is the density of copper, v is the volume of the test samples. In order to validate the accuracy of the above estimation, the porosity Φ of the test sample can also be calculated using the infiltration method:

$$\Phi = \frac{m_2 - m_1}{v \rho_2} \tag{2}$$

where m_2 is the mass of the test samples filled with ethyl alcohol, ρ_2 is the density of ethyl

alcohol. The porosity of all the test samples ranged from 38% to 41% by the calculation. Fig.1 shows the SEM photo of the copper porous structure, in which the particle diameter is in the range of 96-106μm. The average density of the copper porous structure is 5.46 g/cm^3.

Fig. 2 shows the schematic of different surface structures fabricated in this work. As shown in Fig. 2, for the test sample A, it was just a plain surface for comparison purpose; for the test sample B, three rectangular arteries were machined directly into the top surface of the copper pillar, and the copper pillar was covered by a copper porous structure with a thickness of 2.0 mm.   . For the test sample C, three rectangular arteries were made in the bottom surface of the copper porous structure rather than the copper pillar; while for the test sample D, three rectangular arteries were made in the bottom surface of the copper porous structure, and there existed a porous structure with uniform thickness of 0.25 mm between the arteries and the top surface of the copper pillar. In Fig. 2, the diameter of all the copper pillars was 8mm, the thickness of the top copper porous layer was 2 mm, and the width and depth of the rectangular arteries were 1.0 and 1.5 mm respectively.

2.2 Experimental system

Fig. 3 shows schematically the experimental system in this study, which is composed of a high-speed camera, a serpentine reflux condenser, a transparent boiling pool, a copper pillar, a high-frequency electromagnetic induction heater, and a temperature measurement and data acquisition system. The experiments were performed under the standard atmospheric pressure, and deionization (DI) water was employed as the working fluid. Serpentine reflux condenser was employed for cooling the vapor to maintain the liquid level in the pool. The wall of the boiling pool was custom-made of high temperature resistant quartz with an inner diameter of

150mm and height of 140mm to enable a visualization study, and auxiliary heating thermostatic system were employed to maintain the water temperature at a constant value of 100°C. The stainless-steel plate was utilized as a supporting structure, on which a polyetheretherketone (PEEK) plate was introduced to reduce the heat loss from the copper pillar to the stainless steel plate as much as possible. The copper pillar passed through the hole located at the center of the PEEK plate and an O-ring was used to seal the small gap between the copper pillar and the PEEK plate, which can also effectively reduce the possible thermal conduction. The copper pillar was clad by thermal insulation layer made of alumina silicate fiber to decrease the heat loss from the copper pillar to the ambient. The high-frequency electromagnetic induction heater was used to act as the heat source to generate high heat flux, of which the output power can be continuously adjusted within the range of 0-15 kW.

In order to obtain the temperature distribution within the copper pillar, three type K thermocouples (Omega GG-K-30-SLE) with a precision of about ± 0.5 K were placed in the bottom, middle and top of the copper pillar, respectively (Fig. 3). An Agilent 34970A Data Acquisition System was utilized to monitor and record the temperature at a time interval of every 5s,and the Agilent 34970Awas linked to a computer for data display and storage.

2.3 Data reduction and uncertainty analysis

The temperature gradient in the axial direction of the copper pillar (dT/ds), heat flux (q), superheat (ΔT) and evaporation/boiling heat transfer coefficient (h) can be calculated separately through the follow equations.

At the steady state, the temperature gradient dT/ds was estimated using Taylor's backward

series approximation:

$$\frac{dT}{ds} = \frac{3T_{TC1}-4T_{TC2}+T_{TC3}}{2s_0} \tag{3}$$

where T_{TC1}, T_{TC2}, T_{TC3} is measuring point temperature data obtained from the thermocouples, s_0 is the distance from measuring point T_{TC1} to T_{TC2}.

The heat flux on the boiling surface was calculated using Fourier's law of heat conduction equation:

$$q = -\lambda \frac{dT}{ds} \tag{4}$$

where λ is the thermal conductivity, which was measured by hot Disk TPS 2500S，and the tested value is 380W/(m·K).

Once the heat flux on the boiling surface acquired, the superheat and heat transfer coefficient can be calculated as follows:

$$\Delta T = T_w - T_s = T_{TC1} - \frac{qs_0}{\lambda} - T_s \tag{5}$$

$$h = \frac{q}{\Delta T} \tag{6}$$

where T_w is bottom wall temperature of groove structure, T_s is saturated steam temperature of water.

Individual standard uncertainties are considered to estimate the standard deviation of the results, which are calculated using a standard approach as follows:

$$\Delta_q = \sqrt{2\Delta_T^2\left(\frac{\lambda}{2s}\right)^2 + \Delta_s^2\left[\frac{\lambda(T_{TC3}-T_{TC1})}{2s^2}\right]^2} \tag{7}$$

$$\Delta_{\Delta T} = \sqrt{\Delta_T^2 + \frac{q^2}{\lambda^2}\Delta_s^2 + \frac{s_0^2}{\lambda^2}\Delta_q^2} \tag{8}$$

$$\Delta_h = \sqrt{\frac{q^2}{(\Delta T)^4}\Delta_{\Delta T}^2 + \frac{\Delta_q^2}{(\Delta T)^2}} \tag{9}$$

The uncertainty of the temperature measurement (Δ_T)through the thermocouples was within

± 0.5 °C, and the uncertainty of the distance between adjoining thermocouple locations(Δ_s) is approximately ± 0.20 mm. The relative uncertainty is consistently calculated less than 3.0% when the heat flux is larger than 100W/cm². The maximum uncertainty of the heat transfer coefficient is calculated to be less than 5.0% in all the cases. High temperature thermal insulation materials (alumina silicate fiber) were employed to reduce the heat loss from the surface of the copper pillar to the ambient. The thermal conductivity of alumina silicate fiber is about 0.0252 W/(m K), and the total heat loss from the copper pillar to the environment was estimated to be less than 4.0%.

3 Experimental results and discussions

3.1 Comparison among different porous structures

Fig. 5 shows the evaporation/boiling heat transfer performance curves with different surface structures where the heat flux and the HTC represent the heat dissipation capacity and efficiency, respectively.

Fig. 1 (A) shows the boiling heat transfer performance on a plain surface. With the increase of the superheat, both the heat flux and heat transfer coefficient increased. The critical heat flux (CHF) reached ~151 W/cm², after which the boiling entered the film boiling region, resulting in a rapid increase of wall tempertuare due to the presence of vapor film over the surface.

Fig. 1 (B) shows the evaporation/boiling heat transfer performance curves of the structure shown in Fig. 2(B). The heat flux increases with the increase of the superheat; however, the heat transfer coefficient first drops and then rises with the increase of the superheat. This phenomenon should be closely associated with the liquid/vapor distribution in the arteries. At

small heat fluxes, the arteries were filled with liquid, and the boiling mainly occurred at the bottom and side surfaces of the arteries, which is similar to boiling on conventional extended surfaces. . At higher heat fluxes,   more vapor is   generated that reduces the liquid inventory in the arteries, causing an obvious reduction in the effective heat transfer area, i.e., a decrease in the heat transfer coefficient. As the heat flux reaches a threshold value, vapor would completely occupy the arteries, and under this condition, the function of the porous structure began to take effect. The vapor escaping from the liquid/vapor interface and the liquid flowing to the liquid/vapor interface were separated by this porous artery structure.

It should be noted that the highest value of the heat flux in Fig. 4 (b) is not the CHF. When the heat flux continues to rise, the superheat increases   rapidly to more than 150 °C, where the experiments were stopped. Moreover, high superheat is inapplicable for general equipment cooling. This experimental result is consistent with our previous work [31]. This high superheat should be attributed to imperfect contact between the microporous layers and the fins at the top of the copper pillars.

In order to address the   limitations, an improved structure was proposed, as shown in Fig. 2 (C), and the evaporation/boiling heat transfer performance was shown in Fig. 1 (C). In this structure, the solid copper fins were eliminated, and the arteries were made directly in the bottom surface of the porous structure instead. Under this condition, the liquid can be supplied directly to the heating surface. As observed in Fig. 1 (C), the heat flux first increased quickly with the increase of the superheat, and it began to increase slowly after reaching a certain value. The HTC showed a different variation trend: it first increased with the increase of the superheat, and after reaching a peak it began to decrease quickly. The above phenomenon should be closely

associated with the liquid/vapor distribution and vapor movement in the porous artery structure. At small heat fluxes, the microporous copper fins are filled with liquid, and nucleate boiling mainly occurs in the multiple arteries. With the increase of the superheat, both the active nucleation site density and effective heat transfer area increase, which should be responsible for the increase of HTC. At moderate heat fluxes, as more and more vapor is generated, vapor will occupy the whole arteries, and under this condition evaporation mainly occurs at the vertical surface of the microporous copper fins. At high heat fluxes, because the superheat becomes relatively large, vapor bubbles may be generated inside the porous structure and then escape to the multiple arteries. Under this condition, the higher the heat flux, the larger the thickness of the vapor film inside the porous structure, which should be responsible for the decreasing heat transfer coefficient with the increase of the heat flux. From Fig. 4(C), it can be concluded that this porous artery structure can effectively improve the CHF. That is because at high heat fluxes, such a structure can actively formulate the flow paths for liquid replenishment to the liquid/vapor interface and the vapor escaping from the liquid/vapor interface via different routes, with considerably reduced liquid/vapor counter flow.

A similar variation trend in the heat transfer performance was found in structure D, as shown in Fig. 1 (D). Different from the structure C, there exists a thin microporous layer between the copper heating surface and the arteries in structure D. The maximum heat flux obtained in the experiment reached up to 460 W/cm^2. Compared with structure C, the heat flux under the same superheat was improved, and the starting point of the heat transfer coefficient deterioration was delayed. The reason is that on one hand this thin microporous layer can increase the effective heat transfer area; and on the other hand, the liquid can be directly supplied to the heating

surface with the help of the capillary force. This advantage is salient especially at moderate heat fluxes, and the heat transfer coefficient is obviously higher for structure D than that for structure C.

It should be noted that the heat flux growth trend slowed down with the increase of the superheat especially at high heat fluxes, which occurred for both structures C and D. The reason should be attributed to the recession of the liquid/vapor interface in the porous structure. At small and moderate heat fluxes, the superheat was relatively small, and the liquid almost fully filled the porous structure, i.e., no vapor bubbles inside the porous structure were generated. However, with the increase of the superheat, nuclear boiling would occur inside the porous structure, and under this condition, a vapor film would exist in the porous structure adjacent to the heating surface. With the increase of the heat flux, more and more vapor were generated at the liquid/vapor interface, which caused the vapor region to increase and the liquid/vapor interface to recede in the porous structure. The increase of the thickness of the vapor film in the porous structure resulted in an increased heat transfer resistance between the heating surface and the liquid/vapor interface, which should be responsible for the rapid increase of the superheat.

3.2 Effect of structural parameters

In Fig. 1, the boiling heat transfer in structure D shows the best performance, whose maximum heat flux reaches about three times of that on a plain surface. Because the structural parameters play an important role in the boiling heat transfer performance, the effect of relevant geometric parameters of structure D needs to be further studied. The schematic of structure D and the basic parameters are shown in Fig. 2 and Table 1 respectively.

3.2.1 Effect of the thickness of top microporous layer

Fig. 3 (a) and (b) show the superheat dependency of the heat flux and heat transfer coefficient respectively for structure D, where the thickness of top microporous layer includes 1.0, 1.5, 2.0 and 2.5 mm. In the experiment, the artery depth was 2.0 mm, and the thickness of bottom microporous layer was 0.25 mm.

As shown in Fig. 6, the four curves show quite similar variation trend with the increase of the superheat. With the increase of the superheat, the heat flux first increases quickly, then it begins to rise slowly. The maximum heat flux reaches about 460 W/cm^2 when the thickness of top microporous layer is 2.5 mm. As explained earlier in section 3.1, this value is not the CHF.

Fig. 3 clearly shows that with the increase of the thickness of top microporous layer, significant improvement in the pool boiling heat flux and heat transfer coefficient can be achieved. This result is just contrary to our initial expectation. It would be expected that the main function of the top microporous layer is for liquid transport, and an increased thickness of the top microporous layer leads to increased liquid flow resistance. As a result, an increased thickness of the top microporous layer should be adverse to the liquid replenishment to the heating surface, causing reduced boiling heat transfer performance.

For the current experimental results, a possible reason may be presented as follows. The liquid transport through the top microporous layer is in both the vertical and horizontal direction. For the liquid transport in the vertical direction, with a fixed cross sectional area, the increased thickness increase the flow resistance and is obviously adverse to the liquid supply. However, for the liquid transport in the horizontal direction, the increase in the thickness can effectively

increase the cross sectional area, which will be beneficial to the liquid transport and supply. Considering the overall effect of the thickness of the top microporous layer in the range of 1.0-2.5 mm, the increase in the thickness of the top microporous layer can reduce the liquid flow resistance and benefit the liquid replenishment to the heating surface, causing improved boiling heat transfer performance.

In Fig. 6, the boiling heat transfer performance improves monotonously with the increase of the thickness of the top microporous layer; however, it does not mean that simply increasing the thickness of the top microporous layer can always effectively improve the boiling heat transfer performance. That is because when the thickness of the top microporous layer is very large, the liquid flow resistance in the vertical direction will be quite large. Under this condition, the liquid supply through the porous structure to the heating surface will be mainly in the horizontal direction rather than the vertical direction, and the effect of the thickness of the top microporous layer will become very small.

3.2.2 Effect of the artery depth

Fig. 4 (a) and (b) show the effect of artery depth on the heat flux and heat transfer coefficient of structure D respectively, where the artery depth includes 1.0, 1.5 and 2.0 mm. In the experiment, the thickness of top microporous layer and bottom microporous layer were kept constant as 2.0 and 1.0 mm respectively.

As shown in Fig. 4, the effect of artery depth on the evaporation/boiling heat transfer performance for structure D is small, and can be generally ignored when the superheat is relatively small, i.e., $\Delta T < 10\ °C$. While a larger artery depth leads to better evaporation/boiling heat transfer performance at a higher superheat ($\Delta T > 10\ °C$). This result is reasonable as a

larger artery depth means a lower flow resistance of the vapor flowing through it, which can facilitate the vapor removal from the liquid/vapor interface in the porous structure to the pool. The fast and easy vapor escape will result in a smaller layer of vapor region in the microporous structure, corresponding to better evaporation/boiling heat transfer performance. However, too large artery depth will also deteriorate the pool boiling heat transfer performance, because of increased flow resistance of liquid replenishment. Therefore, an optimal artery depth should exist to reach a tradeoff between reduced vapor flow resistance and increased liquid flow resistance.

3.2.3 Effect of the thickness of bottom microporous layer

Fig. 5 (a) and (b) show the superheat dependency of the heat flux and heat transfer coefficient respectively for the structure D, where the thicknesses of the bottom microporous layer is selected as 0.25, 0.5, 0.75 and 1.0 mm. In the experiment, the diameter of the microporous layer was kept at 8.0 mm, and the artery depth and the thickness of top microporous layer were both kept constant at 2 mm.

According to Fig. 5, for the structure D, with the decrease of the thickness of the bottom microporous layer, significant improvement in the pool boiling heat flux and heat transfer coefficient can be achieved. For instance, at a superheat of 30 °C, the heat flux reached about 268 W/cm^2 when the thickness of the bottom microporous layers was 1 mm; while it increased to nearly 449 W/cm^2 when the thickness was decreased to 0.25 mm, i.e., the heat flux was increased to nearly 1.7 times of that with a thickness of 1 mm. That is because the bottom microporous layer plays an important role in the evaporation/boiling heat transfer performance

for this porous artery structure. The reason for heat transfer enhancement is believed to be the reduction in the vapor escape resistance in the bottom microporous layers in the vertical direction, which is also beneficial to the liquid replenishment to the heating surface. In this novel porous artery structure, the bottom microporous layer plays an important role in improving the evaporation/boiling heat transfer performance especially at the inception of boiling, i.e., the superheat is relatively lower at the onset of nucleate boiling. Once the liquid/vapor interface recedes into the copper microporous fins, the role of the bottom microporous layer will disappear. Under this condition, due to the low effective thermal conductivity of the porous layer, the heat transfer resistance increases obviously, causing the deterioration in the heat transfer performance. As shown in Fig. 8 (b), the heat transfer coefficient first increases quickly with the increase of the superheat, after reaching a peak value it begins to drop fast with the increase of the superheat.

In the experiment, a maximum heat flux of 465 W/cm^2 was acquired at the superheat of about 50 °C. It is worth mentioning that this value is not the CHF. Because no vapor column was observed hovering around the porous artery structure in the test. According to our previous experimental results, this porous artery structure can effectively delay the arrival of the CHF utilizing the concept of "phase separation and modulation". However, due to the low thermal conductivity of the copper porous structure, the superheat becomes very large especially at very high heat fluxes. Therefore, this work is dedicated to proposing a novel porous artery structure and optimizing its structural parameters, aiming to achieve a high heat flux heat transfer at an acceptable superheat.

4 Conclusions

In this work, in order to enhance the pool boiling heat transfer performance, different porous artery structures have been proposed based on the concept of "phase separation and modulation". Extensive experimental studies of pool boiling heat transfer in different porous artery structures were performed, and the heat transfer performance was compared and analyzed. In particular, the effects of relevant structural parameters on the boiling heat transfer performance in an innovative porous artery structure were investigated in detail. According to the experimental results and theoretical analysis, some important conclusions have been drawn, as summarized below:

The innovative porous artery structure proposed here can significantly improve the pool boiling heat transfer performance through high-density vapor nucleation sites, capillary-induced liquid replenishment, and the phase separation of liquid/vapor flow. Compared with the boiling heat transfer performance on a plain copper surface, a 200% higher CHF, 144% higher HTC as well as 59% lower superheat at the ONB are demonstrated for this innovative porous artery structure.

The pool boiling heat transfer performance increases with increasing thickness of the top microporous layer, especially at relatively large superheat, which is mainly caused by augmented cross sectional area and reduced liquid flow resistance in the horizontal direction.

There is no obvious relationship between the pool boiling heat transfer performance and artery depth of microporous layer at relatively low superheat. While at relatively high superheat, a larger artery depth contributes to better pool boiling heat transfer performance, which is believed to be due to reduced flow resistance for the vapor removal in the vapor channels.

The pool boiling heat transfer performance increases with decreasing thickness of the bottom microporous layer, especially at moderate and large heat fluxes, which is believed to be due to the reduction in the vapor escape resistance at the bottom microporous layer in the vertical direction.

Acknowledgements

References

[1]   Sur A, Lu Y, Pascente C, Ruchhoeft P, Liu D. Pool boiling heat transfer enhancement with electrowetting.   Int   J   Heat   Mass   Transf   2018;120:202–17. doi:10.1016/j.ijheatmasstransfer.2017.12.029.

[2]   Ji W-T, Zhao C-Y, Zhang D-C, Zhao P-F, Li Z-Y, He Y-L, et al. Pool boiling heat transfer of R134a outside reentrant cavity tubes at higher heat flux. Appl Therm Eng 2017;127:1364– 71. doi:10.1016/j.applthermaleng.2017.08.130.

[3]   Carey VP. Liquid vapor phase change phenomena: an introduction to the thermophysics of vaporization and condensation processes in heat transfer equipment. CRC Press; 2018.

[4]   Zuber N. Hydrodynamic Aspects Of Boiling Heat Transfer (Thesis). Oak Ridge, TN: 1959. doi:10.2172/4175511.

[5]   Lienhard JH, Dhir VK. Hydrodynamic Prediction of Peak Pool-boiling Heat Fluxes from Finite Bodies. J Heat Transfer 1973;95:152. doi:10.1115/1.3450013.

[6]   Kuang-Han C, Ryan E, Evelyn NW. Structured surfaces for enhanced pool boiling heat transfer. Appl Phys Lett 2012;100:241603.

[7]   Kim SJ, Bang IC, Buongiorno J, Hu LW. Surface wettability change during pool boiling of nanofluids and its effect on critical heat flux. Int J Heat Mass Transf 2007;50:4105–16. doi:10.1016/j.ijheatmasstransfer.2007.02.002.

[8]   Wang YQ, Luo JL, Heng Y, Mo DC, Lyu SS. Wettability modification to further enhance the pool boiling performance of the micro nano bi-porous copper surface structure. Int J Heat Mass Transf 2018;119:333–42. doi:10.1016/j.ijheatmasstransfer.2017.11.080.

[9]   Lee JS, Lee JS. Numerical approach to the suppression of film boiling on hot-spots by

radial control of patterned wettability. Int J Multiph Flow 2016;84:165–75. doi:10.1016/j.ijmultiphaseflow.2016.04.021.

[10] Maracy M, Winterton RHS. Hysteresis and contact angle effects in transition pool boiling of water. Int J Heat Mass Transf 1988;31:1443–9. doi:10.1016/0017-9310(88)90253-0.

[11] Liao L. Compositive effects of orientation and contact angle on critical heat flux in pool boiling of water. Heat Mass Transf 2008:180.

[12] Sefiane K. On the role of structural disjoining pressure and contact line pinning in critical heat flux enhancement during boiling of nanofluids. Appl Phys Lett 2006;89:1–4. doi:10.1063/1.2222283.

[13] Kandlikar SG. A Theoretical Model to Predict Pool Boiling CHF Incorporating Effects of Contact Angle and Orientation. J Heat Transfer 2001;123:1071. doi:10.1115/1.1409265.

[14] Kim J, Jun S, Laksnarain R, You SM. Effect of surface roughness on pool boiling heat transfer at a heated surface having moderate wettability. Int J Heat Mass Transf 2016;101:992–1002. doi:10.1016/j.ijheatmasstransfer.2016.05.067.

[15] Fan LW, Li JQ, Zhang L, Yu ZT, Cen KF. Pool boiling heat transfer on a nanoscale roughness-enhanced superhydrophilic surface for accelerated quenching in water. Appl Therm Eng 2016;109:630–9. doi:10.1016/j.applthermaleng.2016.08.131.

[16] Li CH, Li T, Hodgins P, Hunter CN, Voevodin AA, Jones JG, et al. Comparison study of liquid replenishing impacts on critical heat flux and heat transfer coefficient of nucleate pool boiling on multiscale modulated porous structures. Int J Heat Mass Transf 2011;54:3146–55. doi:10.1016/j.ijheatmasstransfer.2011.03.062.

[17] Ahn HS, Lee C, Kim J, Kim MH. The effect of capillary wicking action of micro/nano

structures on pool boiling critical heat flux. Int J Heat Mass Transf 2012;55:89–92. doi:10.1016/j.ijheatmasstransfer.2011.08.044.

[18] Li C, Peterson GP. Parametric Study of Pool Boiling on Horizontal Highly Conductive Microporous Coated Surfaces. J Heat Transfer 2007;129:1465. doi:10.1115/1.2759969.

[19] Surtaev A, Kuznetsov D, Serdyukov V, Pavlenko A, Kalita V, Komlev D, et al. Structured capillary-porous coatings for enhancement of heat transfer at pool boiling. Appl Therm Eng 2018;133:532–42. doi:10.1016/j.applthermaleng.2018.01.051.

[20] Quan X, Dong L, Cheng P. A CHF model for saturated pool boiling on a heated surface with micro/nano-scale structures. Int J Heat Mass Transf 2014;76:452–8. doi:10.1016/j.ijheatmasstransfer.2014.04.037.

[21] Ma X, Cheng P. 3D simulations of pool boiling above smooth horizontal heated surfaces by a phase-change lattice Boltzmann method. Int J Heat Mass Transf 2019;131:1095–108. doi:10.1016/j.ijheatmasstransfer.2018.11.103.

[22] Liter SG, Kaviany M. Pool-boiling CHF enhancement by modulated porous-layer coating: Theory and experiment. Int J Heat Mass Transf 2001;44:4287–311. doi:10.1016/S0017-9310(01)00084-9.

[23] Hwang GS, Kaviany M. Critical heat flux in thin, uniform particle coatings. Int J Heat Mass Transf 2006;49:844–9. doi:10.1016/j.ijheatmasstransfer.2005.09.020.

[24] Wu W, Bostanci H, Chow LC, Hong Y, Su M, Kizito JP. Nucleate boiling heat transfer enhancement for water and FC-72 on titanium oxide and silicon oxide surfaces. Int J Heat Mass Transf 2010;53:1773–7. doi:10.1016/j.ijheatmasstransfer.2010.01.013.

[25] Li C, Peterson GP. Geometric Effects on Critical Heat Flux on Horizontal Microporous

Coatings. J Thermophys Heat Transf 2010;24:449–55. doi:10.2514/1.37619.

[26] Jun S, Kim J, Son D, Kim HY, You SM. Enhancement of Pool Boiling Heat Transfer in Water Using Sintered Copper Microporous Coatings. Nucl Eng Technol 2016;48:932–40. doi:10.1016/j.net.2016.02.018.

[27] Dharmendra M, Suresh S, Sujith Kumar CS, Yang Q. Pool boiling heat transfer enhancement using vertically aligned carbon nanotube coatings on a copper substrate. Appl Therm Eng 2016;99:61–71. doi:10.1016/j.applthermaleng.2015.12.081.

[28] Rishi AM, Gupta A, Kandlikar SG. Improving aging performance of electrodeposited copper coatings during pool boiling. Appl Therm Eng 2018;140:406–14. doi:10.1016/j.applthermaleng.2018.05.061.

[29] Wu W, Du J, Hu X, Wang B. Pool boiling heat transfer and simpli ® ed one-dimensional model for prediction on coated porous surfaces with vapor channels 2002;45:1117–25.

[30] Min DH, Hwang GS, Usta Y, Cora ON, Koc M, Kaviany M. 2-D and 3-D modulated porous coatings for enhanced pool boiling. Int J Heat Mass Transf 2009;52:2607–13. doi:10.1007/978-3-319-61943-9_13.

[31] Zhang K, Bai L, Lin G, Jin H, Wen D. Experimental study on pool boiling in a porous artery structure. Appl Therm Eng 2019;149:377–84. doi:10.1016/j.applthermaleng.2018.12.089.

[32] Penley SJ, Wirtz RA, Advisor D. Structured-Porous Screen Laminate Surface Enhancements for High Heat Flux Boiling of Water under Subatmospheric Pressure 2010.

[33] Li C, Peterson GP. Evaporation/Boiling in Thin Capillary Wicks (II)—Effects of Volumetric Porosity and Mesh Size. J Heat Transfer 2006;128:1320. doi:10.1115/1.2349508.

[34] Rioux RP, Nolan EC, Li CH. A systematic study of pool boiling heat transfer on structured porous surfaces: From nanoscale through microscale to macroscale. AIP Adv 2014;4. doi:10.1063/1.4902343.

[35] Huang G, Liao Z, Xu R, Zhu Y, Jiang P-X. Self-pumping transpiration cooling with phase change for sintered porous plates. Appl Therm Eng 2019;159:113870. doi:10.1016/j.applthermaleng.2019.113870.

[36] Yu DI, Kwak HJ, Noh H, Park HS, Fezzaa K, Kim MH. Synchrotron x-ray imaging visualization study of capillary-induced flow and critical heat flux on surfaces with engineered micropillars 2018:37–42.

[37] Mori S, Maruoka N, Okuyama K. Critical heat flux enhancement by a two-layer structured honeycomb porous plate in a saturated pool boiling of water. Int J Heat Mass Transf 2018;118:429–38. doi:10.1016/j.ijheatmasstransfer.2017.10.100.

[38] Bai L, Zhang L, Lin G, Peterson GP. Pool boiling with high heat flux enabled by a porous artery structure. Appl Phys Lett 2016;108:1–6. doi:10.1063/1.4953574.

[39] Bai L, Zhang L, Guo J, Lin G, Bu X, Wen D. Evaporation/boiling heat transfer characteristics in an artery porous structure. Appl Therm Eng 2016;104:587–95. doi:10.1016/j.applthermaleng.2016.05.113.

[40] Rainho Neto A, Oliveira JLG, Passos JC. Heat transfer coefficient and critical heat flux during nucleate pool boiling of water in the presence of nanoparticles of alumina, maghemite and CNTs. Appl Therm Eng 2017;111:1493–506. doi:10.1016/j.applthermaleng.2016.06.130.

[41] Ray M, Deb S, Bhaumik S. Pool boiling heat transfer of refrigerant R-134a on TiO2 nano wire arrays surface. Appl Therm Eng 2016;107:1294–303.

doi:10.1016/j.applthermaleng.2016.07.080.

[42] Zhong D, Meng J, Li Z, Guo Z. Experimental study of saturated pool boiling from downward facing surfaces with artificial cavities. Exp Therm Fluid Sci 2015;68:442–51. doi:10.1016/j.expthermflusci.2015.06.003.

[43] Das S, Saha B, Bhaumik S. Experimental study of nucleate pool boiling heat transfer of water by surface functionalization with SiO2 nanostructure. Exp Therm Fluid Sci 2017;81:454–65. doi:10.1016/j.expthermflusci.2016.09.009.

[44] Sarafraz MM, Hormozi F, Peyghambarzadeh SM. Pool boiling heat transfer to aqueous alumina nano-fluids on the plain and concentric circular micro-structured (CCM) surfaces. Exp Therm Fluid Sci 2016;72:125–39. doi:10.1016/j.expthermflusci.2015.11.001.

[45] Ho JY, Wong KK, Leong KC. Saturated pool boiling of FC-72 from enhanced surfaces produced by Selective Laser Melting. Int J Heat Mass Transf 2016;99:107–21. doi:10.1016/j.ijheatmasstransfer.2016.03.073.

[46] Kim SH, Lee GC, Kang JY, Moriyama K, Park HS, Kim MH. Heat flux partitioning analysis of pool boiling on micro structured surface using infrared visualization. Int J Heat Mass Transf 2016;102:756–65. doi:10.1016/j.ijheatmasstransfer.2016.06.040.

[47] Sinha-Ray S, Zhang W, Stoltz B, Sahu RP, Sinha-Ray S, Yarin AL. Swing-like pool boiling on nano-textured surfaces for microgravity applications related to cooling of high-power microelectronics. Npj Microgravity 2017;3:9. doi:10.1038/s41526-017-0014-z.

[48] Dai X, Sun N, Nielsen SO, Stogin BB, Wang J, Yang S, et al. Hydrophilic directional slippery rough surfaces for water harvesting. Sci Adv 2018;4:eaaq0919. doi:10.1126/sciadv.aaq0919.

[49] Li CH, Peterson GP. EXPERIMENTAL STUDY OF ENHANCED NUCLEATE BOILING HEAT TRANSFER ON UNIFORM AND MODULATED POROUS STRUCTURES. Front Heat Mass Transf 2010;1. doi:10.5098/hmt.v1.2.3007.

Table captions

Table 1 Basic parameters of the porous artery structure in the experiment
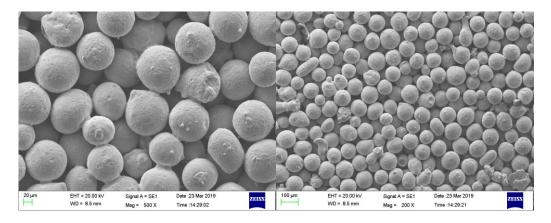
Figure captions

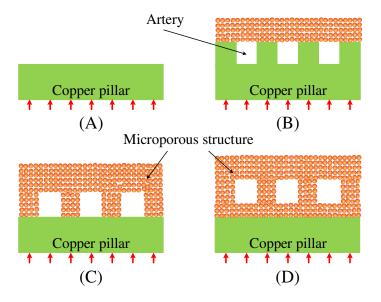Fig. 1 SEM photo of copper porous structure (diameter range 96-106μm)

Fig. 2 Schematic of different test samples in the experiment

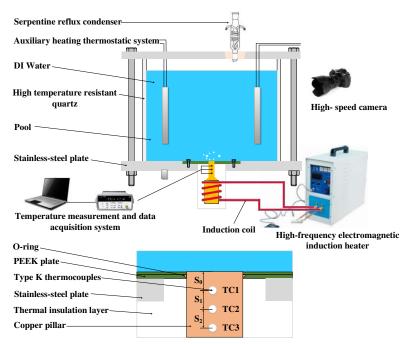Fig. 3 Schematic of the experimental setup

Fig. 4 Boiling heat transfer performance with different surface structures

Fig. 5 Schematic of the porous artery structure

Fig. 6 Effect of the thickness of top microporous layer on the evaporation/boiling heat transfer performance

Fig. 7 Effect of the artery depth of microporous layer on the evaporation/boiling performance

Fig. 8 Effect of the thickness of bottom microporous layer on the evaporation/boiling performance

Table 1 Basic parameters of the porous artery structure in the experiment

Items	Parameter
Diameter of lower part of copper pillar (D_1)/mm	20
Diameter of upper part of copper pillar (D_2)/mm	8.0
Microporous structure diameter (D_3)/mm	8.0
thickness of top microporous layer (H_1)/mm	2.0, 3.0, 4.0
Artery depth (H_2)/mm	1.0, 1.5, 2.0
Thickness of bottom microporous layer (H_3)/mm	0.0, 0.25, 0.5, 0.75, 1.0
Distance (s_0, s_1, s_2)/mm	4.0, 4.0, 4.0
Artery width (W_1)/mm	1.0
Fin width (W_2, W_3)/mm	1.2,1.3

Fig.1 SEM photo of copper porous structure (diameter range 96-106μm)

Fig. 2 Schematic of different test samples in the experiment
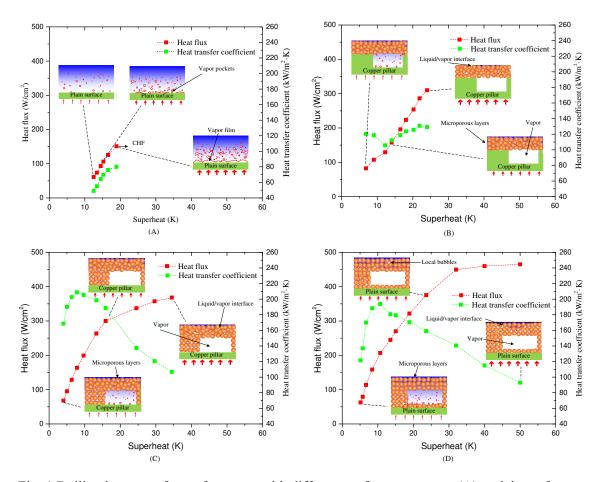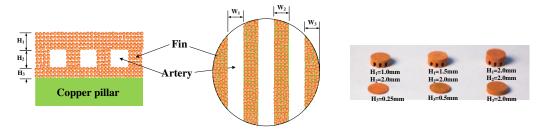
Fig. 3 Schematic of the experimental setup.

Fig. 1 Boiling heat transfer performance with different surface structures: (A) a plain surface, (B) structure B with artery depth 1.5 mm, (C) structure C with artery depth 1.5 mm, and (D) structure D with artery depth 1.5 mm and bottom microporous layer thickness 0.25 mm. (Microporous layer diameter: 8.0 mm, top microporous layer thickness: 2.0 mm).

(A) Multi-layer artery structure (B) Channel section view (C) microporous copper structure
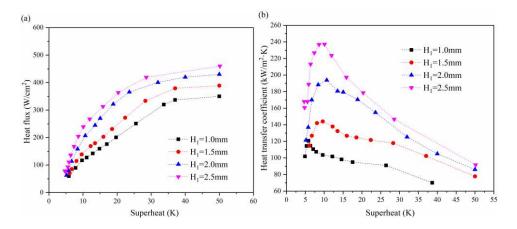
Fig. 2 Schematic of the porous artery structure.

Fig. 3 Effect of the thickness of top microporous layer on the evaporation/boiling heat transfer performance (microporous layer diameter: 8.0 mm, artery depth H_2: 2.0 mm, bottom microporous layer thickness H_3: 0.25 mm, top microporous layer thickness H_1: 1.0, 1.5, 2.0 and 2.5 mm).
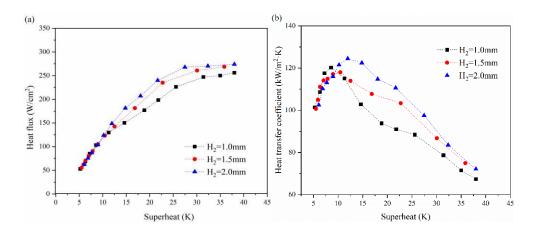
Fig. 4 Effect of the artery depth of microporous layer on the evaporation/boiling performance (microporous layer diameter: 8.0 mm, top microporous layer thickness H_1: 2.0 mm, bottom microporous layer thickness H_3: 1.0 mm, artery depth H_2: 1.0, 1.5 and 2.0 mm).
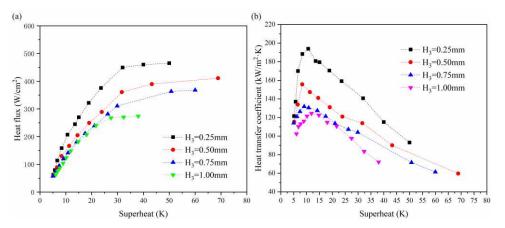

Fig. 5 Effect of the thickness of bottom microporous layer on the evaporation/boiling performance (microporous layer diameter: 8.0 mm, top microporous layer thickness: 2.0 mm, artery depth: 2.0 mm, bottom microporous layer thickness: 0.25, 0.5, 0.75 and 1.0 mm).